Three-dimensional mathematical analysis of particle shape using X-ray tomography and spherical harmonics: Application to aggregates used in concrete

E.J. Garboczi*

National Institute of Standards and Technology, Building and Fire Research Laboratory, 226/B350, Building Materials Division, Gaithersburg, MD 20899, USA

Abstract

The properties of composites made by placing inclusions in a matrix are often controlled by the shape and size of the particles used. Mathematically, characterizing the shape of particles in three dimensions is not a particularly easy task, especially when the particle, for whatever reason, cannot be readily visualized. But, even when particles can be visualized, as in the case of aggregates used in concrete, three-dimensional (3-D) randomness of the particles can make mathematical characterization difficult. This paper describes a mathematical procedure using spherical harmonic functions that can completely characterize concrete aggregate particles and other particles of the same nature. The original 3-D particle images are acquired via X-ray tomography. Three main consequences of the availability of this procedure are mathematical classification of the shape of aggregates from different sources, comparison of composite performance properties to precise morphological aspects of particles, and incorporation of random particles into many-particle computational models. Published by Elsevier Science Ltd.

Keywords: Image and shape analysis; Aggregates; Modeling; X-ray tomography; Spherical harmonics

1. Introduction

Characterizing the shape of particles mathematically is an old and not completely satisfactory activity. Many empirical and analytical classifications of shape, though often based only on two-dimensional (2-D) properties, exist in the literature [1–5]. The differential geometers have derived many tools for characterizing surfaces, such as mean curvature and Gaussian curvature, along with precise definitions of usual quantities like volume and surface area [6]. Physicists have contributed the concept of the moment of inertia tensor [7]. There are also ways to indirectly characterize shape, via the effect of inclusion shape on composite properties when there is a low volume fraction of inclusions in a matrix [8–12]. These effects are often used by polymer scientists and composite material theorists under the name of transport property virial coefficients or dilute limits. The

same kind of shape-based calculations are also found in many other areas of science and engineering, as the problem of particle shape is ubiquitous [8]. These concepts provide a powerful mathematical "tool-kit" with which to characterize the shape of particles. However, applying these mathematical techniques to real, complex, random shapes is a nontrivial task, and much less attention has been paid to this undertaking than to analytical shapes like ellipsoids, torii, cubes, etc. There has of course been a great deal of attention paid to fractal particles [13]. But the kind of particles found in concrete, random but relatively compact particles, seem to have had less attention paid to them in current research.

In the context of aggregates used in concrete, why does one want to mathematically characterize shape? There are at least three reasons. The first is to simply be able to classify different aggregates from different sources, so that their shape differences can be quantified. The second is to be able to quantitatively relate true 3-D aggregate shape characteristics to performance properties. Anecdotal evidence that, for example, "more angular aggregates" give different concrete workability is not enough information on which

* Tel.: +1-301-975-6708; fax: +1-301-990-6891.
E-mail address: edward.garboczi@nist.gov (E.J. Garboczi).

to base a shape optimization of aggregates in concrete. If the shape of particles in a given aggregate type can be mathematically and quantitatively represented in 3-D, inclusion shape–composite property relationships can be developed in a meaningful way.

The third reason to mathematically characterize shape is so that real, random particles can be successfully incorporated into computational models. The random structure of concrete makes it very difficult to be able to model a representative piece of concrete using digital-image-based models, as has been successfully done at the cement particle and paste level [14]. Too many voxels are required, mainly because of the presence of the interfacial transition zone (ITZ) and the wide size range of aggregates present.[1] For example, a representative size sample of a concrete with a maximum aggregate size of about 10 mm should be a cube with a side length of least 50 mm. To adequately resolve the ITZ as well as all the aggregate requires that the minimum voxel size should be at most about 5 μm on an edge, since the ITZ is about 20 μm in width. The minimum sample size in voxels will then be $10,000^3$ or 10^{12}. Storing the model with one byte per voxel would require a computer memory load of 1 TByte, which is uncomfortably large for being able to handle even one model per computer.

To overcome this difficulty, continuum models, called hard-core soft-shell models [15], have been used. These store only the position, orientation, size, and shape information of each particle. If a particle is a sphere, its shape is known and only its diameter need be stored, along with the coordinates of its center. For an ellipsoidal particle, its center, the length of its three semiaxes, and a 3-D vector denoting its orientation have to be stored. Any regular geometric particle can be handled in a similar way. In addition, one must be able to decide if two particles overlap, so that a reasonable concrete model with nonoverlapping aggregates can be generated. For Euclidean particles such as ellipsoids, this can be readily done through fairly simple mathematical functions since the geometry is completely characterized by the orientation and length of the three semiaxes [16–18]. However, real aggregates are not smooth and regular particles, but have random shapes. To be able to insert random particles into these kinds of continuum models requires that each particle be characterized by a limited set of numbers, much fewer than required by digital techniques, where the location of each voxel needs to be stored.

Motivated by the above three factors, the focus of this paper is how mathematical shape analysis of real particles can be successfully performed by acquiring real shapes via X-ray tomography and by analyzing them using spherical harmonic functions. Each particle can be reduced to a limited set of numbers, the coefficients of the spherical harmonic expansion, which fully characterize the particle shape at the resolution of the original image. Continuum models using real aggregates can then be built almost as readily as those involving shapes like spheres and ellipsoids, once the problem of determining overlap for these random particles is overcome.

The kind of spherical harmonic technique described in this paper has been used previously for approximating molecular orbital surfaces [19–21] of proteins and other molecules. It has also been used recently, in a very similar way to that which this paper describes, to characterize the shape of a really *big* rock—an asteriod [22]. A different form of spherical harmonic mathematical techniques is also used in geodesy in the study of the shape of the earth and the shape of satellite orbits [23], an extra-large length-scale shape characterization problem. Similar mathematics as described herein have been used to analyze the shape of aggregates in serial sections [24]. The novel feature of the method used here is that it starts from a 3-D digital image acquired from X-ray tomography. The special features of the spherical harmonic analysis caused by this source of original images will be seen in later sections of the paper. The intention of this paper is to serve as a guide to those desiring to carry out shape analysis using spherical harmonic function techniques. As such, many mathematical details are included in the main text and in appendices to enable practical use to be made of the paper.

The whole procedure of mathematically analyzing shape is far easier to visualize in 2-D than in 3-D. A similar kind of analysis, for 2-D representations of aggregates used in concrete and other shapes, has been carried out previously [25–27]. We review and extend this 2-D formulation here, in order to give a framework of understanding and to introduce concepts, before going into the full 3-D analysis.

2. Two-dimensional illustration

A sample "aggregate" shape to be analyzed is shown in Fig. 1, which was drawn by hand using a drawing program and then saved as a digital file. This file was converted to an ASCII file of one's and two's (one for background, two for object) using a shareware image processing program. The shape is then represented in the computer as a collection of pixels or list of numbers, located at specific sites in the plane. For a real particle, with an actual size, there will be a certain real length associated with the side length of each square pixel.

The center of mass of the object is found using the following equation:

$$\overrightarrow{r}_{CM} = \frac{\sum_i \overrightarrow{r_i}}{\sum_i 1} \tag{1}$$

where the sum over i is a sum over all pixels of the object (pixels with label "2"), the position vector is defined as the
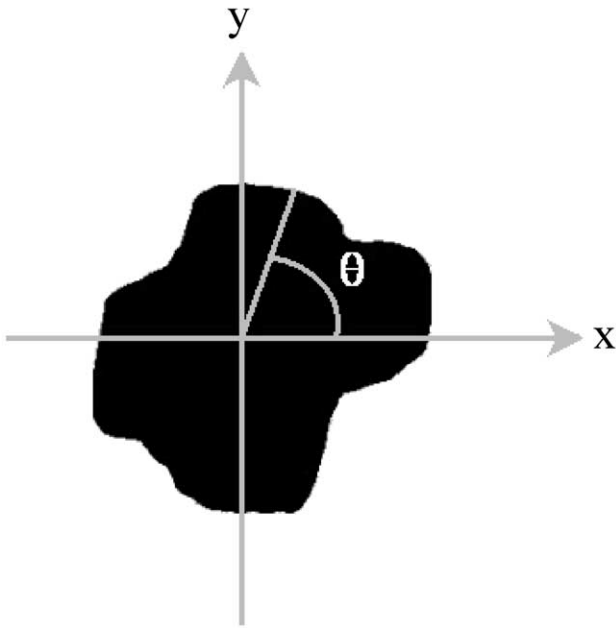

Fig. 1. A 2-D model aggregate shape. The angle θ used in the Fourier analysis is defined. The origin of the coordinate axes is at the center of mass of the object.

vector from the (arbitrary) origin to the center of the pixel of interest, and the symbol in the denominator is the numeral one. The denominator is then simply the area of the object in terms of the number of pixels contained in the object.

The surface of the object is found next, numerically, at a given number of angles by extending a line segment from the center of mass to a point that just crosses the digital surface of the object, which is taken to be the edge of the pixel found at the surface in the direction chosen. The lengths of these line segments are denoted R_n. The angles, between 0 and 2π, are chosen according to a Gaussian quadrature scheme[2] [28] of the order desired, and are illustrated in Fig. 1. This method of finding the surface will cause the numerical surface to contain the small-scale "digital roughness" of the pixellated surface. It is conceivable that some sort of interpolation or smoothing operation could be done at this point, to get rid of the digital roughness to some extent. This has not been done in this paper, for 2-D or for 3-D.

One must note here that this method of finding the surface will only work for a certain class of shapes. Defining this class precisely is left for the 3-D section. For now, it can be simply said that when extending a line segment from the center of mass to the surface, one must not intersect the surface twice. Fig. 2 shows a particle that has two features that would invalidate this procedure: an "overhanging"

feature, and internal porosity that is resolved on the length scale of the pixel size.

The Gaussian quadrature is a method for doing integrals numerically [28]. If a function f is to be integrated from -1 to 1, and a Gaussian quadrature of order N is chosen, then:

$$\int_{-1}^{1} f(x)\mathrm{d}x \approx \sum_{n=1}^{N} f_n w_n \tag{2}$$

where the function is evaluated at the points x_n, $-1 < x_n < 1$, of the Gaussian quadrature, and w_n are the weights of the Gaussian quadrature of that order. In this paper, a 120-point Gaussian quadrature was generally used. If the integration limits are instead a and b, then one uses the linear transformation:

$$x'_n = \frac{1}{2}(b-a)x_n + \frac{1}{2}(b+a) \tag{3}$$

The function is evaluated at these new points, and the sum in Eq. (2) is used to evaluate the integral with the same weights. If $a=0$ and $b=2\pi$, the limits for θ in the surface problem, then this transformation gives the values of θ_n used, for a given value of $0 \le n \le N$.

Now the function $R(\theta)=\{(\theta_n, R_n)\}$ is the length from the center of mass to the surface at an angle θ_n, where θ_n is measured counterclockwise from the x-axis. This function can be constructed to be periodic in θ, by letting $\theta_{N+i} = \theta_i + 2\pi$, and so can be expanded in terms of cosine and sine functions:

$$R(\theta) = \sum_{j=0}^{\infty} [a_j\cos(j\theta) + b_j\sin(j\theta)]. \tag{4}$$

Note that the value of b_0 can be taken to be zero, as sin(0) equals zero identically. Also note that Eq. (4) could be
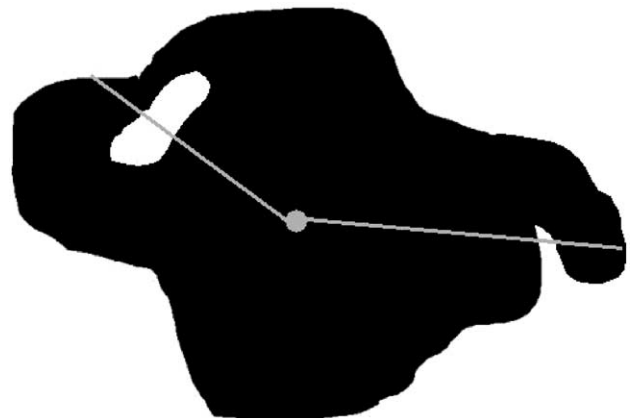

Fig. 2. A 2-D model aggregate shape that illustrates the features that are not allowed in the mathematical analysis, including resolved internal porosity, and an "overhanging" region, giving a nonsingle-valued surface, as measured by directed segments from the center of mass.

---

[2] Note that the Gaussian quadrature points and the Gaussian curvature are related only by the name of the single brilliant mathematician who thought of them both.

written in terms of a complex exponential, which combines the sine and cosine terms.

The values of a_j and b_j are given by the integrals:

$$a_j = \frac{1}{2\pi} \int_0^{2\pi} R(\theta)\cos(j\theta)d\theta$$

$$b_j = \frac{1}{2\pi} \int_0^{2\pi} R(\theta)\sin(j\theta)d\theta \qquad (5)$$

These integrals are straightforward to do, since the values of θ_n were chosen according to the Gaussian quadrature procedure, and so are "ready-made" to do the integrals. Fig. 3 provides a plot of the values of a_j and b_j vs. j found for the shape shown in Fig. 1. Note that, while there is fluctuation, the values of the coefficients tend to decrease as the value of j increases. By $j = 20$, the coefficients have become small enough to be negligible. After this point, higher order values of j are just trying to match the pixel-to-pixel digital structure of the exterior of the object, which is probably not an important or realistic part of the real shape.

Fig. 4 shows the computed shape of the object for different numbers of Fourier coefficients used, i.e.,

$$R(\theta) \approx \sum_{j=0}^{N}[a_j\cos(j\theta) + b_j\sin(j\theta)]. \qquad (6)$$

Note that the a_0 coefficient is a measure of the average circular size of the object, as can be seen also in Eq. (5), and the other coefficients ($j \geq 1$) can be thought of as perturbing the average circular surface to match the correct shape.
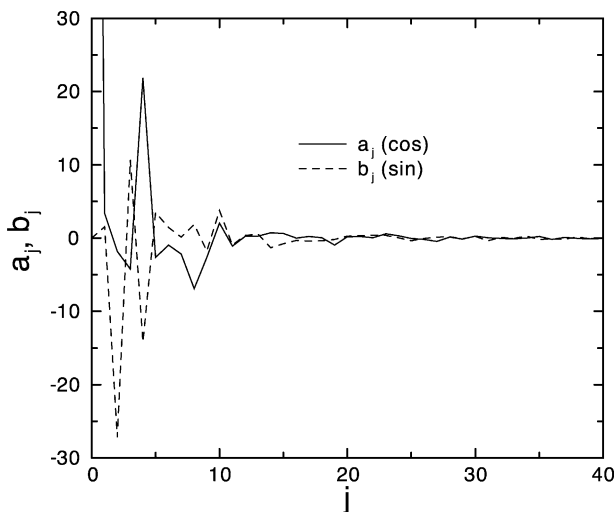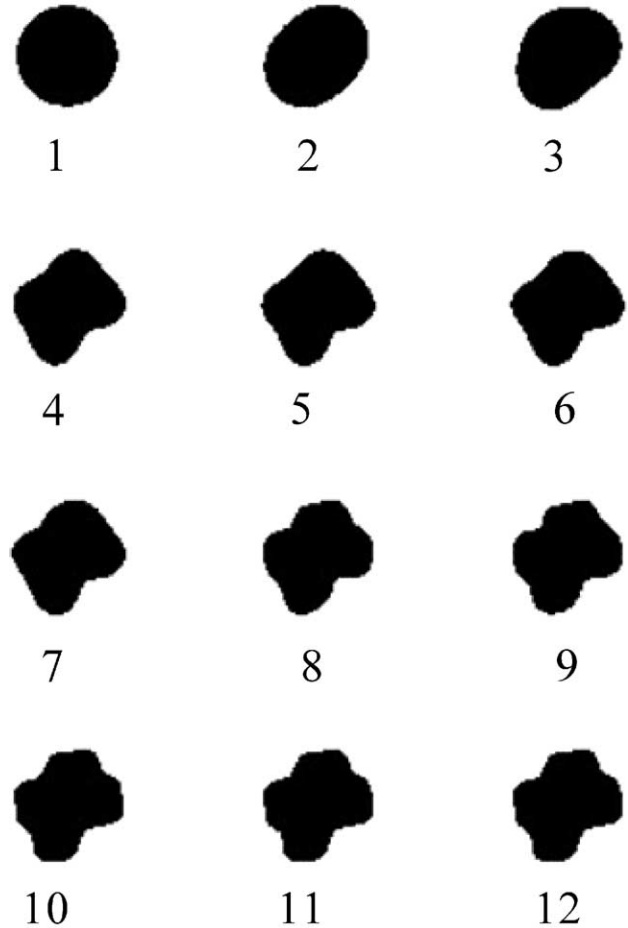

Fig. 4. The shape of the analyzed image of Fig. 1 for different numbers of cos and sin coefficients used to recreate the shape. The numeric labels in the figure are equivalent to the j values in the previous figure.

Fig. 5 shows the computed area of the shape, using the expansion, as a function of how many expansion coefficients were used. The equation for the area A of a given shape, using N coefficients, is [29]:

$$A = \frac{1}{2}\int_0^{2\pi}[r(\theta)]^2 d\theta = \pi a_0^2 + \frac{\pi}{2}\sum_{j=1}^{N}(a_j^2 + b_j^2) \qquad (7)$$

Note that by $N = 10$ or so, the area has reached its asymptotic value, which is less than the digital value by only 0.1%. The digital area is just the number of the pixels times the area of each pixel. In this model case, the area of each pixel is taken to be unity. The slight disagreement reflects the fact that the surface of the object was only sampled at a finite number of points. Choosing surface points according to a higher order Gaussian quadrature would cause this error to be smaller, as long as the numerical accuracy of the computer was not exceeded. However, one does not want to totally reproduce the digital details of the pixellated surface, as presumably these details
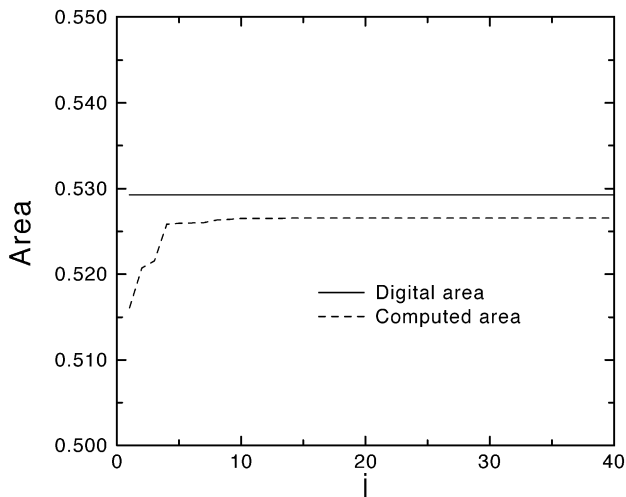

Fig. 3. The cos and sin coefficients as a function of the index j for the shape shown in Fig. 1. The value of $a_0 \approx 200$ is off the vertical scale so that the smaller coefficients could be seen.

Fig. 5. The computed area of the shape shown in Fig. 2 as a function of the index j.

are not real, but are only an artifact of using square pixels to represent a true curved surface. So there is an upper limit on how fine one wants to resolve the surface.

The technique described for 2-D has been: image acquisition, numerical surface determination, and then Fourier analysis. In 3-D, the image is (1) generated using X-ray tomography, (2) acquired numerically, and then (3) analyzed with spherical harmonic functions, which are the 3-D equivalent of the Fourier series. In the case of the asteroid mentioned earlier [22], the surface was numerically sampled using laser range finder measurements made by an orbiting satellite. The X-ray tomography and particle image acquisition step for the procedure in 3-D is described next.

3. X-ray tomography and particle acquisition

X-ray computed tomography (CT) [30] offers a nondestructive technique for visualizing features in the interior of opaque solid objects to obtain digital information on their 3-D geometry and topology. In the case of concrete, the aggregates used in the concrete can be visualized inside a concrete cylinder.

The aggregate images to be shown in this paper were taken from an X-ray tomograph of a real concrete sample captured using an X-ray CT system located at the Turner Fairbank Highway Research Center [31]. Concrete prisms having a 75×75 mm cross-sectional area, a water/cement mass ratio of 0.5, with quartz sand used as the fine aggregate and limestone used as the coarse aggregate, were made and used. The gray scale image that comes from the tomographic process was thresholded to a black and white image by recovering the known volume of aggregates contained in the sample.

Fig. 6 shows a 270^3 pixel portion of the final result, cut out of the original image (this size was chosen only for

convenience, as much larger samples can be handled). Aggregates (high density) in Fig. 6 appear white, while the matrix, consisting of cement paste and unresolved fine aggregate particles, appears black. The large flat areas on the aggregates showing on the faces of the cube are from the cut through the sample, and are not part of the real image. The voxels are cubes with dimensions of approximately 0.4 mm per side. The physical size of the concrete sample shown in Fig. 6 is then about $108 \times 108 \times 108$ mm. The image shown in Fig. 6 represents preliminary work at a fairly coarse resolution, but is adequate for the purpose of illustrating the mathematical algorithms described in subsequent sections. Much higher resolution, of about $20-40$ μm per voxel side, is possible.

Given that a 3-D multiaggregate image has been obtained, one can proceed to extract individual particles. Ideally, when carrying out this procedure routinely, the image should be taken of a system with a fairly low volume percent of aggregate, say 20%, so that on the average, most particles are not near each other. The image in Fig. 6, however, was of a real concrete at a practical aggregate volume percentage (around 60%). Because of this fact, when the 3-D image was made, many particles appeared to be in contact. This was because of the fairly coarse resolution of the image, which would make many close but not touching contacts to appear as real contacts. Converting the gray scale image to a binary image can also cause some artificial particle contacts. This situation was handled with a simple erosion and dilation algorithm [32], which broke apart the tenuously connected aggregates, without significantly changing their size or shape.

A "burning" algorithm was used to identify single particles. It is quite analogous to the algorithm used in
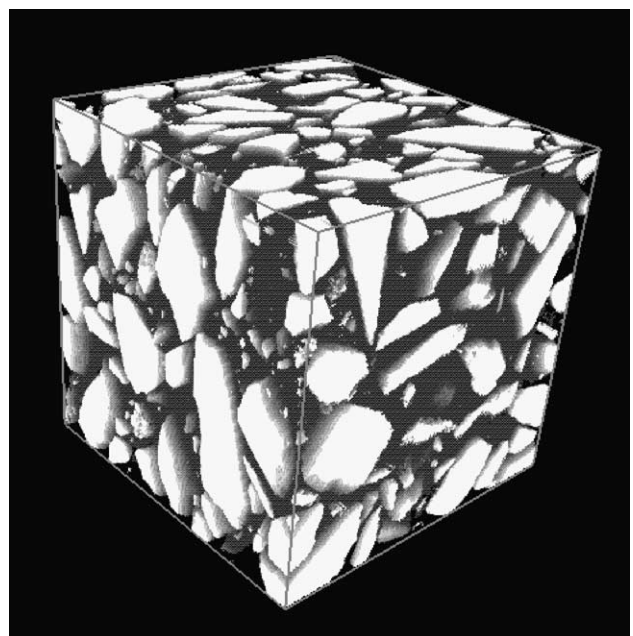

Fig. 6. A 270^3 voxel piece of a tomographic image of a concrete material.

percolation studies, both in digital, pixel-based models [33], and in continuum model studies [12], for determining the connectivity of extended clusters. Imagine a 3-D cube of pixels, like that shown in Fig. 6, where each pixel is labeled either matrix (1) or particle (2). Assume that enough precautions have been taken, either physically, by keeping the volume fraction of aggregate low, or numerically, by using some kind of erosion/dilation routine, that no particle is touching any other particle. We will also stay away from the boundaries and so not allow any artificially "sliced" particles to be identified. Scan through the image until a pixel is found that has label "2." This corresponds to the single black pixel shown in Fig. 7, which shows a model particle in 2-D. Now find all nearest neighbors (back–front, left–right, up–down) of this pixel that also have label "2." In Fig. 7, the first round of this neighbor identification will come up with those pixels labelled a. Save the locations of these pixels, and then find all neighbors of the a pixels that also have the same label (b in Fig. 7). Iterate this process until no more pixels of label "2" can be found. The collection of pixels (voxels in 3-D) found constitutes a single particle.

The main image is now systematically examined for particles, which when found are stored in a simple database. The coordinates of each voxel, relative to the center of mass of the particle in which it was found, are stored. Any particle can easily be regenerated by placing its center of mass at any location in a 3-D digital image. These coordinates are used to generate a surface function of the 3-D particle, which can be analyzed with spherical harmonic functions, as is described in Section 4.
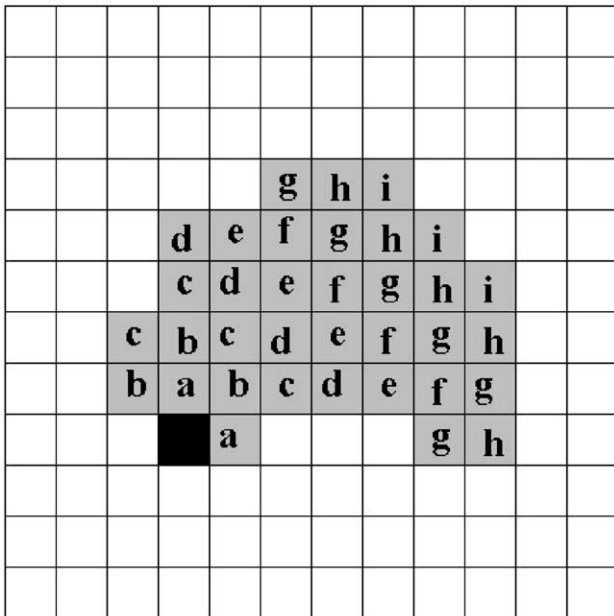

Fig. 7. A 2-D illustration of how the burning algorithm for particle identification works. The black pixel is found first, then the a neighbors, then the b neighbors, and finally the i neighbors, completing the particle.

4. Spherical harmonic mathematical analysis

The procedure to generate the 2-D surface of a 3-D particle is qualitatively the same as in generating the 1-D surface of a 2-D particle. Starting from the center of mass, which is defined in 3-D similarly to 2-D, line segments are positioned from the center of mass to the surface at various angles (θ_i, ϕ_j), where these angles are the usual spherical polar coordinates [34]. The length of these line segments, denoted $R_{ij}(\theta_i, \phi_j)$, are found numerically at the values of the angles corresponding to the points of a double Gaussian quadrature, one for each angle, where R_{ij} is the distance from the center of mass to a surface point along the direction defined by (θ_i, ϕ_j). A surface point is defined as a point on the surface of a pixel. The Cartesian coordinates of these surface points, with the origin defined at the particle center of mass, are:

$$x_{ij} = R_{ij}\sin(\theta_i)\cos(\phi_j)$$

$$y_{ij} = R_{ij}\sin(\theta_i)\sin(\phi_j)$$

$$z_{ij} = R_{ij}\cos(\theta_i). \tag{8}$$

Now is the time to state more clearly what kinds of particles can be handled accurately by this kind of analysis. We require that the shape to be "star-like" [19–21]. For a shape to be star-like, any line segment whose one endpoint is the center of mass and the other endpoint is on the surface must be totally contained in the shape itself. Therefore, there can be no "overhangs" or "bubbles" in the shape, as was depicted in Fig. 2. This requirement should be satisfied by almost all aggregates, because the grinding process, whether natural, in a riverbed, or artificial, in a rock-crushing machine, should break down any "overhanging" bits, and rocks usually do not have internal porosity large enough to show up in a tomograph that uses the resolutions of tens of micrometers per pixel. Many aggregates do have internal porosity, but as long as it is smaller than the resolution of the tomograph, it will not be seen in the particle images created by the tomograph. If there are any of these features in the X-ray tomographic images, the spherical harmonic analysis process will create a "valley" from the internal bubble to the real surface, since encountering the bubble surface first as a line segment proceeds from the center of mass will cause it to be interpreted as the real particle surface. The signature of this happening will be a significant difference between the digital volume and the volume as computed from the spherical harmonic expansion. All the examples of aggregates that will be shown in this paper are star-like, as judged from the original tomographic image, and did not have internal porosity.

Once a star-like particle has been obtained, and surface points $R_{ij}(\theta_i, \phi_j)$ found, then spherical harmonic analysis (the

3-D equivalent of 2-D Fourier analysis) can be applied. The key equation in the spherical harmonic analysis process is the following, where $r(\theta,\phi)$ is any smooth function defined on the unit sphere ($0 \leq \theta \leq \pi$, $0 \leq \phi \leq 2\pi$) [34–36]:

$$r(\theta, \phi) = \sum_{n=0}^{\infty} \sum_{m=-n}^{n} a_{nm} Y_n^m(\theta, \phi). \tag{9}$$

For these assumptions, the spherical expansion exists and converges. In our case, $r(\theta,\phi)$ is given numerically by $(\theta_i, \phi_j, R_{ij})$. The function $Y_n^m(\theta,\phi)$ is called a spherical harmonic function, and is given by:

$$Y_n^m(\theta, \phi) = \sqrt{\left(\frac{(2n+1)(n-m)!}{4\pi(n+m)!} \right)} P_n^m(\cos(\theta)) e^{im\phi} \tag{10}$$

The functions $P_n^m(x)$ are called associated Legendre functions, and are a set of orthogonal polynomials found in quantum mechanics [35] and many other fields. Appendix A lists the associated Legendre functions up to order $n = 8$. In this case, $x = \cos(\theta)$. Values of higher order associated Legendre functions can be found using recursion relations [34]. These recursion relations are available in user-ready Fortran programs like DXLEGF, a part of the SLATEC numerical package [37]. Using explicit formulae for the associated Legendre functions up to $n = 8$ helps give more accuracy to this recursion process, hence the listing herein. Using explicit formulas up to higher values of n would be still more helpful, but the algebra to calculate these quickly becomes tedious.

The computed surface points are then used to calculate the coefficients a_{nm}, which depend on both n and m according to the following definition:

$$a_{nm} = \int_0^{2\pi} \int_0^{\pi} d\phi d\theta \sin(\theta) r(\theta, \phi) Y_n^{m*} \tag{11}$$

where the asterisk denotes the complex conjugate. Choosing each angle to correspond to the points of a Gaussian quadrature makes evaluation of these integrals straightforward. In 3-D, a 120-point Gaussian quadrature was used for each angle, so that Eq. (11) was evaluated by summing over $120^2 = 14,400$ points. In some cases, a 240-point Gaussian quadrature, with 57,600 points, was used.

A set of coefficients, once determined, then serve as a complete, within numerical error, mathematical characterization of the aggregate particle. Much of the later sections of this paper examines error analysis of how well the expansion works for simple shapes, by direct numerical comparison to analytically known quantities, and by visual and numerical comparison to the original random digital particles from the tomograph.

Many properties of the shape can be computed once the spherical harmonic expansion is known. These include volume, surface area, mean and Gaussian curvature both at a point of the surface and integrated over the surface, and the moment of inertia tensor, as defined below. The volume and moment of inertia can also be computed directly from the digital image by counting voxels.

The equation for the volume of the shape in polar coordinates is particularly simple and is given by:

$$V = \int_0^{2\pi} \int_0^{\pi} \int_0^{r(\theta,\phi)} r^2 \sin(\theta) dr d\theta d\phi \tag{12}$$

where the integral is over all angles and for values of r between the origin at the center of mass and the surface, $r(\theta,\phi)$, which is given by the computed expansion of Eq. (9). The r integral can be analytically performed, and the resulting integral is then, in terms of the function $r(\theta,\phi)$,

$$V = \frac{1}{3} \int_0^{2\pi} \int_0^{\pi} r^3(\theta, \phi) \sin(\theta) d\theta d\phi. \tag{13}$$

The equations for the surface area and integrated curvatures involve some auxiliary terms that are defined in differential geometry. These are given below [21]. A useful way of denoting points on the surface of the particle is by the vector $\vec{X}$, which is the Cartesian coordinates of surface points. The components of $\vec{X}$ ($X_1 = x$, $X_2 = y$, $X_3 = z$) are similar to those given in Eq. (8), and derivatives of $\vec{X}$ are denoted by a subscript.

There are eight auxiliary quantities that are useful in analyzing surfaces, and they are all built out of components of $\vec{X}$ and the surface normal vector $\hat{n}$, which is given by:

$$\hat{n} = \frac{\vec{X_\theta} \times \vec{X_\phi}}{\left| \vec{X_\theta} \times \vec{X_\phi} \right|}. \tag{14}$$

The differential surface area element, $d\Lambda$, which is the area of the patch of surface at $r(\theta,\phi)$, is given by:

$$d\Lambda = S d\theta d\phi, \quad S = \left| \vec{X_\theta} \times \vec{X_\phi} \right| \tag{15}$$

The parameters E, F, and G are given by:

$$E = \vec{X_\theta} \cdot \vec{X_\theta}$$

$$F = \vec{X_\theta} \cdot \vec{X_\phi}$$

$$G = \vec{X_\phi} \cdot \vec{X_\phi} \tag{16}$$

The parameters L, M, and N are:

$$L = -\overrightarrow{X_\theta} \cdot \hat{n}_\theta$$

$$M = \frac{1}{2}\left(\overrightarrow{X_\theta} \cdot \hat{n}_\phi + \overrightarrow{X_\phi} \cdot \hat{n}_\theta\right)$$

$$N = -\overrightarrow{X_\phi} \cdot \hat{n}_\phi. \tag{17}$$

Since the function $r(\theta,\phi)$ is known in terms of a spherical harmonic expansion, and the Cartesian coordinates of the surface are known in terms of $r(\theta,\phi)$, all the above derivatives can be taken and the results for all the various surface parameters given in terms of derivatives of $r(\theta,\phi)$. In the following, these derivatives of $r(\theta,\phi)$ are denoted by the notation:

$$r = r(\theta, \phi)$$

$$\frac{\partial r(\theta, \phi)}{\partial \theta} = r_\theta$$

$$\frac{\partial r(\theta, \phi)}{\partial \phi} = r_\phi$$

$$\frac{\partial^2 r(\theta, \phi)}{\partial \phi^2} = r_{\phi\phi}$$

$$\frac{\partial^2 r(\theta, \phi)}{\partial \theta^2} = r_{\theta\theta}$$

$$\frac{\partial^2 r(\theta, \phi)}{\partial \phi \partial \theta} = r_{\phi\theta} = r_{\theta\phi} \tag{18}$$

The actual functional form of these derivatives, in terms of the spherical harmonic expansion (Eq. (9)) are given in Appendix B.

The surface area S_A is an integral over θ and ϕ of the differential surface element in Eq. (15). The parameter S, using the spherical harmonic expansion, is:

$$S = r[r_\phi^2 + r_\theta^2 \sin^2(\theta) + r^2 \sin^2(\theta)]^{1/2} \tag{19}$$

so that the surface area S_A is:

$$S_A = \int_0^{2\pi} \int_0^\pi r[r_\phi^2 + r_\theta^2 \sin^2(\theta) + r^2 \sin^2(\theta)]^{1/2} d\theta d\phi \tag{20}$$

The parameters E, F, and G are given by:

$$E = r_\theta^2 + r^2$$

$$F = r_\theta r_\phi$$

$$G = r_\phi^2 + r^2 \sin^2\theta \tag{21}$$

The parameters L, M, and N involve vector products of the derivatives of the components of $\overrightarrow{X}$ and $\hat{n}$ (see Eq. (17)). The components of $\hat{n}$ and derivatives of the components are fairly complicated, so that the explicit forms of L, M, and N are not given in the text. The derivatives of the components of $\overrightarrow{X}$ and $\hat{n}$ are listed in Appendix B, however. Eq. (17) can then be used to write out the equations for L, M, and N, and numerically evaluate them and the values of other quantities that depend on them.

The local mean curvature H is defined as the arithmetical mean of the two principal curvatures at each point on the surface [21], and is given by:

$$H = \frac{EN + GL - 2FM}{2(EG - F^2)} = H(\theta, \phi) \tag{22}$$

The Gaussian curvature K, which is another measure of surface curvature, is the geometric mean of the two principal curvatures at each point on the surface:

$$K = \frac{LN - M^2}{EG - F^2} = K(\theta, \phi). \tag{23}$$

The mean curvature, averaged over the surface and weighted by the differential surface element, is defined here as h, where:

$$h = \frac{1}{S_A} \int_0^{2\pi} \int_0^\pi H d\Lambda. \tag{24}$$

The parameter h has units of inverse length, since the mean curvature H has units of inverse length. If h is then inverted, the resulting length depends on the size and shape of the object considered. One should note that the term "integrated mean curvature" is often referred to in the literature as Eq. (24) without the normalizing factor of S_A^{-1} [38].

An interesting property of the Gaussian curvature, when similarly integrated over the surface, is that:

$$k = \frac{1}{4\pi} \int_S K d\Lambda = 1 \tag{25}$$

when the object under consideration is topologically equivalent to a sphere. This is the case for the star-like aggregate considered here. "Topologically equivalent to a sphere" means if the object were made out of very pliant

rubber, it could be deformed, without ripping or puncturing, into a sphere. Eq. (25) is then a very useful quality control check for the spherical harmonic expansion procedure. Also, one should be able to make a judgement of when "enough" terms in the expansion have been computed, by when this criterion is fulfilled.

The terms of the moment of inertia tensor I_{ij}, where i, $j = 1, 2, 3$, are given by [7]:

$$I_{ij} = \int_V \rho(\vec{r}) d^3 r (\delta_{ij} r^2 - x_i x_j) \tag{26}$$

where $\rho(\vec{r})$ is the density of the object, δ_{ij} is the Kronecker delta (zero for $i \neq j$ and 1 when $i = j$), the integral is over the entire particle volume V, and $I_{ji} = I_{ij}$. If the mass density of the object is uniform, so that $\rho = M/V$ (total mass divided by total volume), then using the definition of the polar coordinates in Eq. (8), and performing the r integral like in Eq. (13), the I_{11} integral, for example, transforms to:

$$I_{11} = \frac{M}{5V} \int_0^{2\pi} \int_0^{\pi} r^5(\theta, \phi) \sin(\theta)[1 - \sin^2(\theta)\cos^2(\phi)] d\theta d\phi \tag{27}$$

The remaining components of the moment of inertia tensor can be found in Appendix B.

Even though the result of Eq. (25) exists for any aggregate shape that would be considered, it is important to have other checks as well, to establish the limitations and perform error analysis on the spherical harmonic expansion procedure. This error analysis is carried out next using various analytical shapes.

5. Error analysis using ellipsoids

One can analyze the limitations of the spherical harmonic shape analysis method, as developed in this paper, by applying it to shapes for which all the properties of interest are known analytically. A sphere is a known shape, but its analysis is trivial, since only the coefficient a_{00} is non-zero when a spherical harmonic expansion like Eq. (9) is carried out for a sphere. An ellipsoid, however, has many non-zero values for its coefficients, and has known analytical results for its properties. Ellipsoids of revolution in particular were used, as there exists closed-form solutions for the properties of these shapes in terms of elementary functions [38–40] (see Appendix C). The shapes used were a 5:1 prolate and a 1:5 oblate ellipsoid of revolution. By this is meant ellipsoids with axes in the ratio of 1:1:5 and 5:5:1. Various digital versions, using different digital resolutions, were made of these shapes and the numerical procedures tested on them. Only results for the prolate ellipsoid will be shown, as the results were similar for the oblate ellipsoid. Each ellipsoid was centered on a voxel center, and a voxel was counted to

be a part of the ellipsoid if its center were inside the analytical limits of the ellipsoid.

Fig. 8 shows the volume and surface area for a 5:1 prolate ellipsoid as a function of the number of spherical harmonic coefficients used (in terms of N). The solid lines are the exact analytical result for an ellipsoid with axis dimensions, in terms of voxel length, of (21, 21, 105). The expansion results become very close to the exact analytical results by about $N = 12$. Fig. 9 shows, for the same ellipsoid, the values of I_{11} and I_{33}. The graph also shows h^{-1}, which is a combined measure of the average size and shape of the object. Again, the results basically become equal to the exact analytical results by about $N = 12$. Although not shown, the value of k stays very close to 1 (much less than 1% difference) for all values of N up to 24.

It is important to note that the spherical harmonic coefficients are being generated from the digital realization of the ellipsoid, not the exact formula. By using the exact formula for an ellipsoid centered on the origin and aligned with the coordinate axes,

$$\frac{x^2}{a^2} + \frac{y^2}{a^2} + \frac{z^2}{c^2} = 1 \tag{28}$$

where again $2a = 21$ and $2c = 105$, one can easily show that the exact value of $r(\theta, \phi)$ is given by:

$$r(\theta, \phi) = a^2 c [a^2 c^2 \sin^2(\theta) + a^4 \cos^2(\theta)]^{-1/2}. \tag{29}$$

Since $r(\theta, \phi)$ is a function of θ only, this implies that the only spherical harmonic coefficients that are non-zero
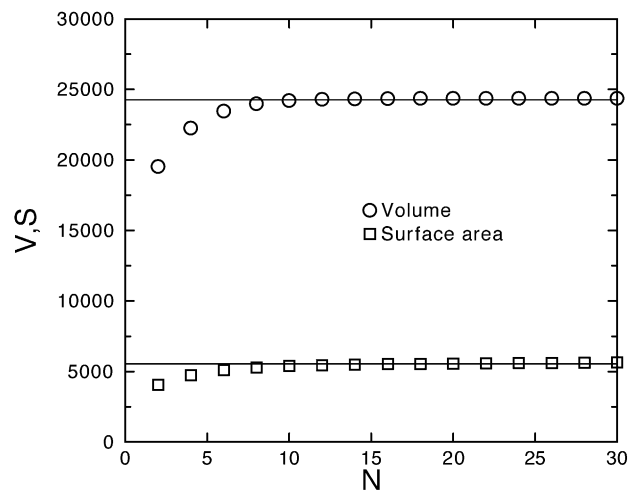

Fig. 8. The volume and surface area of a 5:1 prolate ellipsoid of revolution as a function of the number of spherical harmonic functions, N, used in the expansion. The expansion was made from a digital image of the ellipsoid that was $21 \times 21 \times 105$ pixels in extent. The solid lines are the exact result for a continuum ellipsoid.
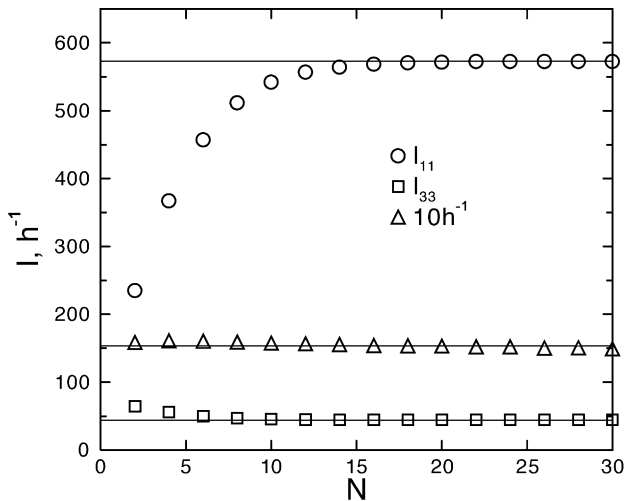
Fig. 9. The two independent components of the moment of inertia tensor (described in text) and the reciprocal of the surface-area-weighted integrated mean curvature for a 5:1 prolate ellipsoid of revolution, plotted as a function of the number of spherical harmonic functions, N, used in the expansion. The expansion was made from a digital image of the ellipsoid that was $21 \times 21 \times 105$ pixels in extent. The solid lines are the exact result for a continuum ellipsoid.

have $m = 0$. And since $r(\theta, \phi)$ is even in θ, only a_{n0} with n even are non-zero. This is found to be approximately true for the numerical results, which are generated from the digital image of the (21, 21, 105) ellipsoid, not the exact value of $r(\theta)$.

Table 1 shows the values of $a(n, 0)$ vs. n for the numerical and the exact analytical results (generated using the exact value of r). One can see, as N gets into double digits, an increasing amount of disagreement between the exact and numerical results. The disagreement should increase for a coarser resolution ellipsoid image and decrease for a finer resolution image.

The above was an analysis of the error incurred when using a varying number of coefficients on a fixed digital resolution image. One also has to address the question of changing digital resolution on the computed shape parameters of particles, such as volume and surface area. What is the resolution needed, for a given number of spherical harmonic coefficients, for a digital object to give accurate

Table 1
The exact and numerical values of the a_{n0} coefficients in the spherical harmonic expansion for an ellipsoid of revolution with axes in the ratio 21:21:105

n	Coefficient	Exact	Numerical	% difference
0	$a_{0\ 0}$	52.0237	52.1800	0.3
2	$a_{2\ 0}$	19.7127	19.6905	− 0.1
4	$a_{4\ 0}$	9.9545	9.9199	− 0.35
6	a_6	5.5475	5.5526	0.1
8	$a_{8\ 0}$	3.2408	3.2673	0.8
10	$a_{10\ 0}$	1.9461	1.9885	2.2
12	$a_{12\ 0}$	1.1899	1.1228	− 5.6

results in the spherical harmonic expansion? A similar analysis is performed, but with coarser resolution digital ellipsoids, comparing the spherical harmonic-computed quantities with their exact analytical counterparts.

Fig. 10 shows the volume and surface area for a 5:1 prolate ellipsoid as a function of the number of spherical harmonic coefficients used (in terms of N), for an ellipsoid that now has axis dimensions, in terms of voxels, of 11:11:55. The expansion results become very close to the exact analytical results by about $N = 12$, although there is a
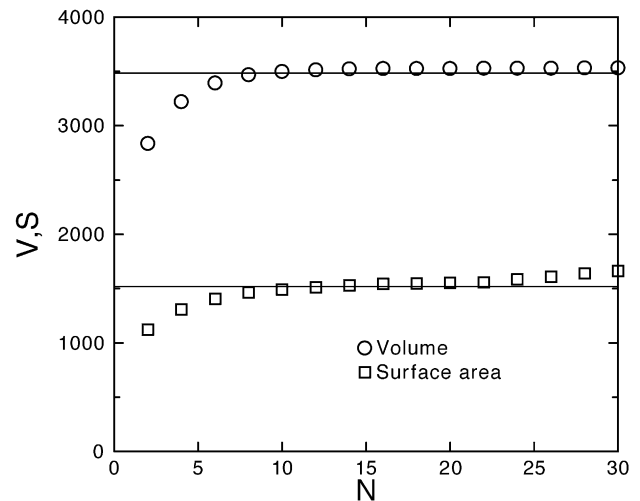

Fig. 10. The volume and surface area of a 5:1 prolate ellipsoid of revolution as a function of the number of spherical harmonic functions, N, used in the expansion. The expansion was made from a digital image of the ellipsoid that was $11 \times 11 \times 55$ pixels in extent. The solid lines are the exact result for a continuum ellipsoid.
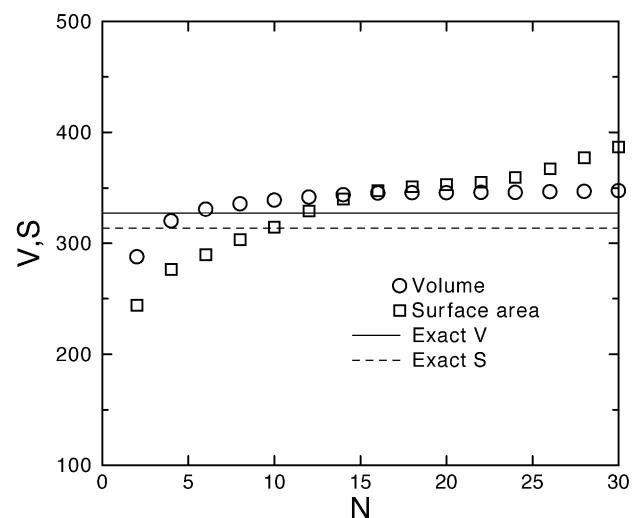

Fig. 11. The volume and surface area of a 5:1 prolate ellipsoid of revolution as a function of the number of spherical harmonic functions, N, used in the expansion. The expansion was made from a digital image of the ellipsoid that was $5 \times 5 \times 25$ pixels in extent. The solid and dashed lines are the exact result for a continuum ellipsoid.

small amount of "drift" upwards past the exact quantities for higher values of N. Fig. 11 shows the same quantities, but for an ellipsoid with axis dimensions of 5:5:25. It is interesting to note that there is a flat part of the graph starting again at about $N = 12$. The spherical harmonic results go significantly above the exact lines as N increases beyond about 20. If one were to stop at $N = 12$, the volume would be off by 5% and the surface area would be too high by about 8%.

One can analyze the lowest resolution ellipsoid data in several ways. First, the digital volume is itself inaccurate at this resolution. For this ellipsoid, which has axis dimensions of 5:5:25, the exact volume is 327.25. The digital volume is 349. For $N = 12$, the volume calculated using the spherical harmonic expansion, which was itself taken from the digital image, is only off from the digital volume by -1.4%. Second, one can examine the integrated Gaussian curvature of Eq. (25) to see at how high a value of N should the spherical harmonic expansion be trusted. By $N \geq 14$, the value of k is more than 2% different from 1. So the "best" results for this shape are at $N = 12$, which agrees with the flat part of the graph. Also, it is clearly seen that the spherical harmonic expansion faithfully follows the digital image shape, not the analytical shape. Since in the case of images of aggregates derived from X-ray tomographs, only the digital image is available, this fact is comforting.

When considering the surface area of digital images in the past [43], it was found that the digital surface area, obtained by counting voxel faces, was too high. For a sphere, it is too high by a value of about 3/2. For many random pore structures, not based on a sphere, this value also holds true [44]. However, by examining Table 2, one can see that the ratio of the digital surface area to the true surface area does depend on the shape of the ellipsoid, oblate, or prolate, but only weakly on the resolution used, at least down to the lowest resolution shown in the table. But, as could be seen in Fig. 8, the spherical harmonic expansion gave a surface area that was quite close to the exact value for the prolate ellipsoid. So, in this case, there is higher accuracy in using the expansion than in correcting the digital surface area, since the correction is not universal, but depends on the ellipsoid shape. For example, if the aspect ratio was 1 for both prolate and oblate shapes, so that

they were spheres, the equivalent ratio would be 1.5. For an aspect ratio of 20, the oblate ratio is 1.085 and the prolate ratio is 1.371.

How the prolate ratio changes with shape is hard to see intuitively. The range of variation for the oblate shapes is easier to see. As an ellipsoid of revolution becomes very oblate, its surface area approaches the surfaces of two circles (see the oblate surface area formula in Appendix C). The digital area of a circle is very accurate [33], and so the ratio should go to unity in this limit, and vary between 3/2 and 1 in between the sphere and extreme oblate limit.

Now that the accuracy of the spherical harmonic technique has been analyzed, one can go on to illustrate its use on images of real aggregates.

6. Some results on real aggregates

Real aggregate shapes were obtained via the burning algorithm from Fig. 6. Visual comparisons will be made first between numerical image data obtained directly from the X-ray tomograph and images of particles that have been reconstructed from the spherical harmonic expansion.

Figs. 12 and 13 show side-by-side views of real particles (mottled dark gray) taken directly from the X-ray tomograph, and the corresponding reconstructed particle (light gray). By "reconstruction" is meant that an image rendering program was used to triangulate the particle surface as defined by the spherical harmonic expansion. The image pairs can be seen to match each other closely in both figures. How the spherical harmonic expansion effectively interpolates the surface can be qualitatively seen in these image pairs. This simple visual comparison is reassuring, but not conclusive, as to the accuracy of the spherical harmonic expansion on random shapes.

A more quantitative study can be done of the random particles shown in Figs. 12 and 13. But, the most important question in this analysis, which must be addressed first, is the following: what is the "right" answer against which the spherical harmonic analysis is to be compared? There are no analytically correct quantities with which to compare as was the case for ellipsoids, except for the result of Eq. (25), which is true for all shapes considered herein.

Only the digital volume of the original image exists against which to compare the spherical harmonic-derived volume. The moment of inertia tensor can also be computed using the centers of the voxels to numerically evaluate Eq. (26). In general, terms involving volume integrals are easily computed for the digital shapes by performing the appropriate sums over the voxels.

However, terms that are calculated by surface integrals are difficult to compute for digital images. The surfaces of digital images are composed of square tiles oriented along the coordinate axes (digitally rough), and overcount the surface area by some amount up to a factor of 3/2, as

Table 2
The digital and exact surface areas and their ratio for three oblate and three prolate digital ellipsoids of different resolutions

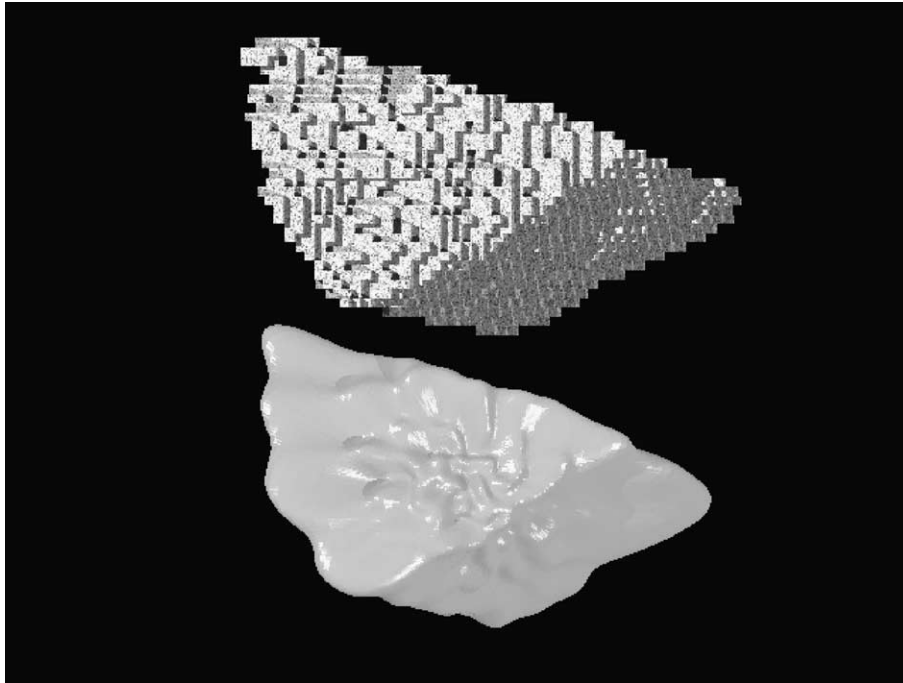| Shape	Ellipsoid axes	Digital S_A	Exact S_A	Ratio of digital S_A to exact S_A
Prolate	5:5:25	446	313.7	1.422
Prolate	11:11:55	2118	1518.3	1.395
Prolate	21:21:105	7694	5533.7	1.390
Oblate	25:25:5	1382	1073.6	1.287
Oblate	55:55:11	6678	5196.4	1.285
Oblate	105:105:21	24,366	18,938.8	1.287

Fig. 12. Comparing the digital image taken directly from the original X-ray tomograph (mottled gray) (digital volume = 9175 voxels), with the spherical harmonic expansion reconstruction (shiny gray). A slight surface texture has been added to the tomographic image in order to see the digital detail more clearly.

was discussed above. It is really not possible to integrate over a digital surface without using some kind of interpolation scheme. The spherical harmonic expansion essentially interpolates the digital surface. If there were to be a physical measurement of aggregate surface area, the number computed using the spherical harmonic expansion would be better to compare with rather than the digital measure of surface area, as has been seen previously. Of
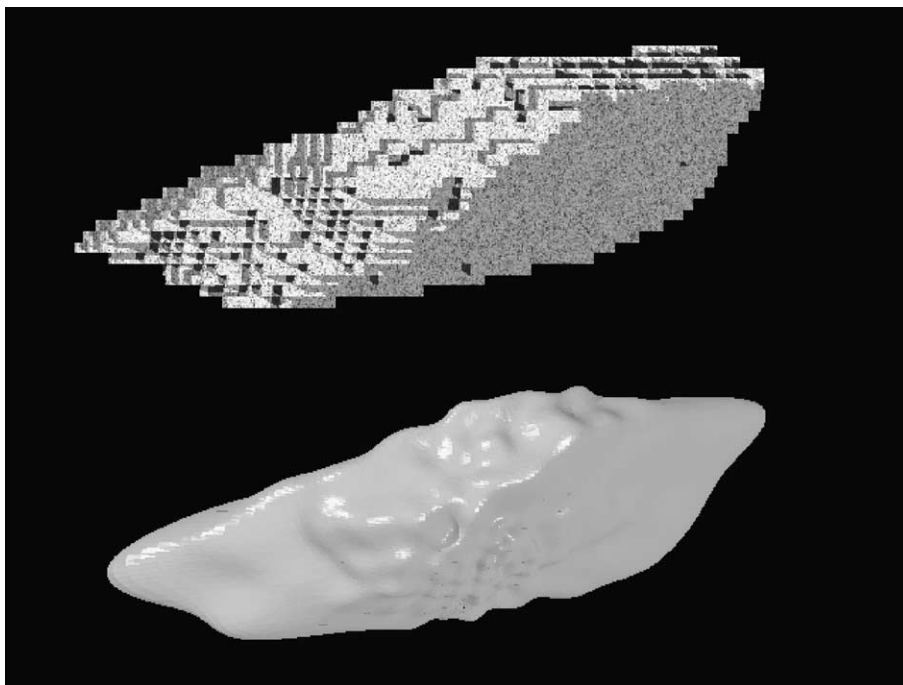

Fig. 13. Comparing the digital image taken directly from the original X-ray tomograph (mottled gray) (digital volume = 9061 voxels), with the spherical harmonic expansion reconstruction (shiny gray). A slight surface texture has been added to the tomographic image in order to see the digital detail more clearly.

course, the value of k must be unity for any random or nonrandom shape aggregate like those considered here. Because of these facts, it is only meaningful, in the following, to compare spherical harmonic results for volume and I_{ij}, since they are computed via volume integrals, and k, since it is independent of shape, to their digital equivalents.

With these limitations in mind, one can proceed to do similar calculations with the real particles as with the ellipsoids, looking at the effect of the number of spherical harmonic terms used and at the number of Gaussian quadrature points used to originally compute the surface analysis (surface interpolation) and spherical harmonic coefficients, and then used to compute the various properties of the particle considered. These two sets of Gaussian quadratures are kept equal to each other, and are varied together below.

First, consider the particle shown in Fig. 12. One can compute the components of the moment of inertia tensor using the spherical harmonic expansion, as a function of the number of terms used in the expansion. Fig. 14 shows these components, as well as the "exact" numbers computed directly from the digital image. By the time N gets past 12 or so, there is quite good agreement (1%) between all five pairs of terms. The term I_{22} is not shown, as it was similar in value to I_{33}. Even the negative term, I_{13}, shows good agreement between digital calculation and spherical harmonic expansion.

Fig. 15 shows the results for the volume and k for the particle shown in Fig. 13, as a function of the number of terms taken in the spherical harmonic expansion. The volume has been normalized by the "exact" digital volume. Both a 120-point and a 240-point Gaussian quadrature were used to compute the volume and k integrals. The value of k deviates significantly from unity by $N = 10$, for the 120-point Gaussian quadrature, but is close to unity all the way
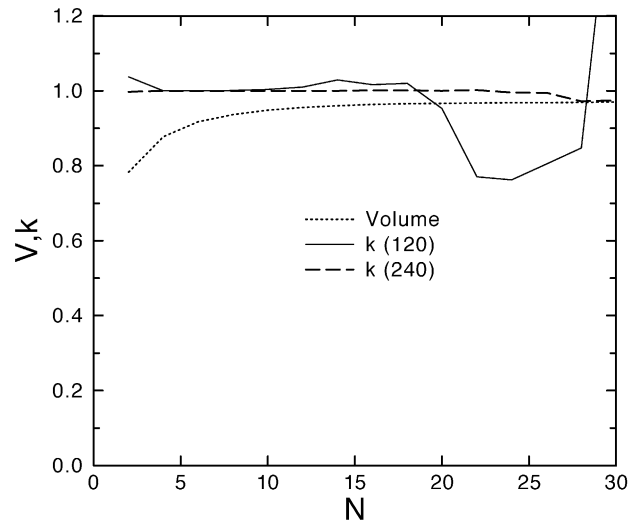
Fig. 15. The volume, normalized by the particle volume of 9061 voxels for the particle shown in Fig. 13, and the value of k, as a function of the number of terms, N, used in the spherical harmonic expansion. The two k curves are Gaussian quadratures of 120 and 240 points used for all aspects (surface determination, calculation of spherical harmonic coefficients, calculation of particle properties) of the spherical harmonic expansion calculation.

to $N = 25$ when the 240-point quadrature was used. Surprisingly, the volume was relatively insensitive to the differing number of quadrature points, so only the 120-point case is shown. This example shows how the integrated value of the Gaussian curvature can be used for "quality control" of the mathematical analysis.

7. Future work and discussion

This paper has shown that the technique of acquiring 3-D particle images via X-ray tomography, extracting the individual particles computationally from the image, and analyzing the particle in terms of a spherical harmonic expansion, can completely mathematically characterize the shape of random particles. Using the expansion, one can systematically build aggregate databases, similarly to how cement image databases are being built [41] inside the Virtual Cement and Concrete Testing Laboratory [42]. These databases can be used to analyze the aggregate particles from a certain quarry or made by a certain process, making use of the quantitative shape information that comes from the spherical harmonic expansion.

One must remember the limitations of the technique, balancing the digital resolution of the original tomographic image against the number of Gaussian quadrature points used to determine the surface and spherical harmonic coefficients and to calculate the various particle properties. Careful analysis of these effects leads to estimates of the uncertainties involved in the process.

One can also estimate what is the smallest aggregate particle that can be handled with the X-ray tomographic
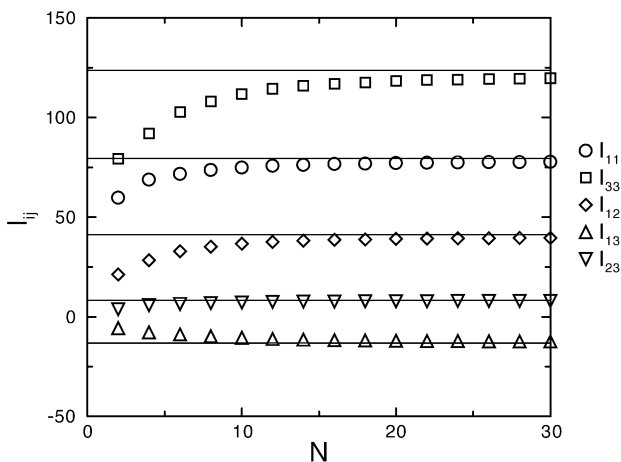

Fig. 14. The components of the moment of inertia tensor, for the particle shown in Fig. 12, as a function of the number of spherical harmonic terms, N, used in the expansion of the particle shape. The solid lines are the components as calculated directly from the X-ray tomographic digital image, and serve as the "exact" check on the spherical harmonic result.

resolution available. Suppose that the resolution of the X-ray tomographic unit is x_r micrometers per voxel edge length. From the ellipsoid work carried out above, the smallest particle, in terms of voxels, that can reasonably approximate the shape of a real particle, is probably about 5–10 voxels on a side. Taking 5 as the lower limit, the size of the particle is at most $5x_r$ μm in extent. If $x_r = 50$ μm, then the smallest particle that can be analyzed is 250 μm in size, corresponding to a standard mesh size between no. 100 and no. 50. This is a small sand particle, in terms of usual aggregate classifications, but not the smallest routinely encountered.

In an X-ray tomographic apparatus, the resolution x_r can be reduced, but at the expense of using a smaller sample. Roughly speaking, whatever the physical size of sample is, the 3-D tomographic image will be N^3 in size, where N is typically 512 or 1024. So the value of x_r is just the sample size divided by N. Decreasing the sample size will decrease the image resolution, but at the expense of having to use smaller aggregates. To acquire images of the entire aggregate range used in concrete, coarse to fine, would probably require at least two samples, one large and one small.

The first and second proposed use of the spherical harmonic technique, as discussed in the introduction, was to analyze and classify the shapes of individual particles and compare their shape quantitatively to performance properties. This can now be done. A range of aggregate images can be captured via X-ray tomography, and the particles acquired and stored in a database automatically using the modified burning algorithm. A spherical harmonic expansion can be generated for each one, and the expansion coefficients analyzed and correlated versus performance properties, since they are an exact measure of shape. Much more research needs to be done in this regard, since this paper only makes the technique available—applications need to be carried out.

The third proposal was to use the analyzed shapes to build models using these particles in a similar way to how spheres and ellipsoids could be handled before. This task is not yet complete. What mainly needs to be done is to be able to take two particles, place them at arbitrary locations and at arbitrary rotations, and then decide whether or not these two particles overlap. The mathematics of placing and rotating particles is contained in Ref. [21], and so just needs to be implemented for this program. Deciding whether two particles overlap, which is necessary for building up real concrete models, is somewhat harder and remains to be worked out. Some insight will come from analyses of ellipsoidal contact functions [16–18], which are mathematical functions that give an unambiguous answer, >1 or <1, whether two ellipsoids overlap or not. This task is achievable, as in principle all the information about the surface is analytically contained in the spherical harmonic expansion. Progress has been made in accomplishing this task, and will be reported in a forthcoming publication.

As has been seen from the literature, the spherical harmonic expansion technique for reconstructing particle shape has been used for satellite orbits and the shape of the earth ($\sim 10^7$ m in size), for the shape of asteroids ($\sim 10^4$ m in size), and for the shape of molecular orbitals ($\sim 10^{-10}$ m in size). The size scale of the application discussed here, aggregate shapes, lies in between these extreme length scales. But, in all these applications, only the size scale and physical problem differs—the mathematical techniques are the same. So it is rather satisfying to use these techniques at the size scale of aggregates employed in concrete. The combination of X-ray tomography and spherical harmonic analysis allows the routine 3-D analysis of aggregate shapes, completing the multiscale picture of "particle" shape for a very wide range of length scales.

Acknowledgments

Appendix A. List of associated Legendre functions

Let $x = \cos(\theta)$ and $s = \sqrt{1 - x2}$. The associated Legendre functions $P_n{}^m = P_n{}^m(x)$ are listed below, for $n = 0, 8$ and $m = 0, n$, in Table 3 ($n = 0, 5$) and Table 4 ($n = 6, 8$). The

Table 3
List of associated Legendre polynomials from $n=0$ to $n=5$

n	m	Function
0	0	1
1	0	x
1	1	s
2	0	$\frac{1}{2}(3x^2 - 1)$
2	1	$3xs$
2	2	$3(1 - x^2)$
3	0	$\frac{1}{2}[x(5x^2 - 3)]$
3	1	$\frac{3}{2}(5x^2 - 1)s$
3	2	$15x(1 - x^2)$
3	3	$15s^3$
4	0	$\frac{1}{8}(35x^4 - 30x^2 + 3)$
4	1	$\frac{5}{2}(7x^3 - 3x)s$
4	2	$\frac{15}{2}(7x^2 - 1)(1 - x^2)$
4	3	$105xs^3$
4	4	$105s^4$
5	0	$\frac{1}{8}[x(63x^4 - 70x^2 + 15)]$
5	1	$\frac{15}{8}[s(21x^4 - 14x^2 + 1)]$
5	2	$\frac{105}{2}[x(1 - x^2)(3x^2 - 1)]$
5	3	$\frac{105}{2}[s^3(9x^2 - 1)]$
5	4	$945xs^4$
5	5	$945s^5$

Table 4
List of associated Legendre polynomials from $n = 6$ to $n = 8$

n	m	Function
6	0	$\frac{1}{16}(231x^6 - 315x^4 + 105x^2 - 5)$
6	1	$\frac{21}{8}[x(33x^4 - 30x^2 + 5)s]$
6	2	$\frac{105}{8}[s^2(33x^4 - 18x^2 + 1)]$
6	3	$\frac{315}{2}(11x^2 - 3)xs^3$
6	4	$\frac{945}{2}[s^4(11x^2 - 1)]$
6	5	$10395xs^5$
6	6	$10395x^6$
7	0	$\frac{1}{16}[x(429x^6 - 693x^4 + 315x^2 - 35)]$
7	1	$\frac{7}{16}[s(429x^6 - 495x^4 + 135x^2 - 5)]$
7	2	$\frac{63}{8}[xs^2(143x^4 - 110x^2 + 15)]$
7	3	$\frac{315}{8}[s^3(143x^4 - 66x^2 + 3)]$
7	4	$\frac{3465}{2}[xs^4(13x^2 - 3)]$
7	5	$\frac{10,395}{2}[s^5(13x^2 - 1)]$
7	6	$135,135xs^6$
7	7	$135,135s^7$
8	0	$\frac{1}{128}(6435x^8 - 12,012x^6 + 6930x^4 - 1260x^2 + 35)$
8	1	$\frac{9}{16}[xs(715x^6 - 1001x^4 + 385x^2 - 35)]$
8	2	$\frac{315}{16}[s^2(143x^6 - 143x^4 + 33x^2 - 1)]$
8	3	$\frac{3465}{8}[xs^3(39x^4 - 26x^2 + 3)]$
8	4	$\frac{10,395}{8}[s^4(65x^4 - 26x^2 + 1)]$
8	5	$\frac{135,135}{2}[xs^5(5x^2 - 1)]$
8	6	$\frac{135,135}{2}[s^6(15x^2 - 1)]$
8	7	$2,027,025xs^7$
8	8	$2,027,025s^8$

associated Legendre functions with $m = -M < 0$ are simply given in terms of the equivalent functions with $M > 0$ according to:

$$P_n^m = P_n^{-M} = (-1)^M \frac{(n-M)!}{(n+M)!} P_n^M. \quad (30)$$

Appendix B. Mathematical quantities for spherical harmonic shape analysis

B.1. Derivatives of the surface function $r(\theta, \phi)$

The values of the various derivatives of the surface function $r(\theta, \phi)$ are given below, in terms of the spherical harmonic expansion and using the recursion relations given in Ref. [34], where the auxiliary parameter f_{nm} is:

$$f_{nm} = \sqrt{\left(\frac{(2n+1)(n-m)!}{4\pi(n+m)!}\right)} \quad (31)$$

Note that for negative values of m, one uses the definitions of associated Legendre functions with negative values of m given above in Appendix A.

$$r_\phi = \sum_{n=0}^{\infty} \sum_{m=-n}^{n} (im)a_{nm}Y_n^m(\theta, \phi)$$

$$r_{\phi\phi} = \sum_{n=0}^{\infty} \sum_{m=-n}^{n} -m^2 a_{nm}Y_n^m(\theta, \phi)$$

$$r_\theta = \sum_{n=0}^{\infty} \sum_{m=-n}^{n} \frac{-a_{nm}f_{nm}}{\sin\theta}[(n+1)\cos\theta P_n^m$$
$$- (n-m+1)P_{n+1}^m]e^{im\phi}$$

$$r_{\theta\theta} = \sum_{n=0}^{\infty} \sum_{m=-n}^{n} \frac{a_{nm}f_{nm}}{\sin^2\theta}[(n+1+(n+1)^2\cos^2\theta)P_n^m$$
$$- 2\cos\theta(n-m+1)(n+2)P_{n+1}^m$$
$$+ (n-m+1)(n-m+2)P_{n+2}^m]e^{im\phi}$$

$$r_{\phi\theta} = r_{\theta\phi} = \sum_{n=0}^{\infty} \sum_{m=-n}^{n} \frac{-ima_{nm}f_{nm}}{\sin\theta}[(n+1)\cos\theta P_n^m$$
$$- (n-m+1)P_{n+1}^m]e^{im\phi}. \quad (32)$$

B.2. Surface normal and surface vector quantities

The components of the unit surface normal $\hat{n}$ are:

$$n_x = S^{-1}[rr_\phi\sin\phi - rr_\theta\sin\theta\cos\theta\cos\phi + r^2\sin^2\theta\cos\phi]$$

$$n_y = S^{-1}[-rr_\phi\cos\phi - rr_\theta\sin\theta\cos\theta\sin\phi + r^2\sin^2\theta\sin\phi]$$

$$n_z = S^{-1}[rr_\theta\sin^2\theta + r^2\cos\theta\sin\theta] \quad (33)$$

and the derivatives of the surface vector $\vec{X}$ are:

$$\frac{\partial\vec{X}}{\partial\phi} = (r_\phi\sin\theta\cos\phi - r\sin\theta\sin\phi, \ r_\phi\sin\theta\sin\phi$$
$$+ r\sin\theta\cos\phi, \ r_\phi\cos\theta) \quad (34)$$

$$\frac{\partial\vec{X}}{\partial\theta} = (r\cos\theta\cos\phi + r_\theta\sin\theta\cos\phi, \ r\cos\theta\sin\phi$$
$$+ r_\theta\sin\theta\sin\phi, \ r_\theta\cos\theta - r\sin\theta). \quad (35)$$

The derivatives of the components of $\hat{n}$ with respect to ϕ are given by the following formula, where $i = x, y, z$:

$$\frac{\partial n_i}{\partial\phi} = S^{-1}\left[a_i - b_i\left(\frac{r_\phi}{r} + \frac{c_i}{S^2}\right)\right] \quad (36)$$

where the functions a_i, b_i, and c_i are:

$$a_1 = r_\phi^2 \sin\phi + rr_{\phi\phi}\sin\phi + rr_\phi\cos\phi - r_\phi r_\theta\sin\theta\cos\theta\cos\phi$$
$$- rr_{\theta\phi}\sin\theta\cos\theta\cos\phi + rr_\theta\sin\theta\cos\theta\sin\phi$$
$$+ 2rr_\phi\sin\theta\cos\phi$$
$$- r^2\sin^2\theta\sin\phi$$

$$b_1 = rr_\phi\sin\phi - rr_\theta\sin\theta\cos\theta\cos\phi + r^2\sin^2\theta\cos\phi$$

$$c_1 = r^2(r_\phi r_{\phi\phi} + r_\theta r_{\theta\phi}\sin^2\theta + rr_\phi\sin^2\theta$$

$$a_2 = -r_\phi^2\cos\phi - rr_{\phi\phi}\cos\phi + rr_\phi\sin\phi - r_\phi r_\theta\sin\theta\cos\theta\sin\phi$$
$$- rr_{\theta\phi}\sin\theta\cos\theta\sin\phi - rr_\theta\sin\theta\cos\theta\cos\phi$$
$$+ 2rr_\phi\sin^2\theta\sin\phi + r^2\sin^2\theta\cos\phi$$

$$b_2 = -rr_\phi\cos\phi - rr_\theta\sin\theta\cos\theta\sin\phi + r^2\sin^2\theta\sin\phi$$

$$c_2 = c_1$$

$$a_3 = r_\phi r_\theta\sin^2\theta + rr_{\theta\phi}\sin^2\theta + 2rr_\phi\sin\theta\cos\theta$$

$$b_3 = rr_\theta\sin^2\theta + r^2\sin\theta\cos\theta$$

$$c_3 = c_1 \tag{37}$$

The derivatives of the components of $\hat{n}$ with respect to θ are given by a formula similar to that for ϕ:

$$\frac{\partial n_i}{\partial\theta} = S^{-1}\left[a_i - b_i\left(\frac{r_\theta}{r} + \frac{c_i}{S^2}\right)\right] \tag{38}$$

where the functions a_i, b_i, and c_i are:

$$a_1 = r_\theta r_\phi\sin\phi + rr_{\theta\phi}\sin\phi - r_\theta^2\sin\theta\cos\theta\cos\phi$$
$$- rr_{\theta\theta}\sin\theta\cos\theta\cos\phi - rr_\theta\cos^2\theta\cos\phi$$
$$+ rr_\theta\sin^2\theta\cos\phi + 2rr_\theta\sin^2\theta\cos\phi$$
$$+ 2r^2\sin\theta\cos\theta\cos\phi$$

$$b_1 = rr_\phi\sin\phi - rr_\theta\sin\theta\cos\theta\cos\phi + r^2\sin^2\theta\cos\phi$$

$$c_1 = r_\phi r_{\theta\phi} + r_\theta r_{\theta\theta}\sin^2\theta + rr_\theta\sin^2\theta + r_\theta^2\sin\theta\cos\theta$$
$$+ r^2\sin\theta\cos\theta$$

$$a_2 = -r_\phi r_\theta\cos\phi - rr_{\theta\phi}\cos\phi - r_\theta^2\sin\theta\cos\theta\sin\phi$$
$$- rr_{\theta\theta}\sin\theta\cos\theta\sin\phi - rr_\theta\cos^2\theta\sin\phi + rr_\theta\sin^2\theta\sin\phi$$
$$+ 2rr_\theta\sin^2\theta\sin\phi + 2r^2\sin\theta\cos\theta\sin\phi$$

$$b_2 = -rr_\phi\cos\phi - rr_\theta\sin\theta\cos\theta\sin\phi + r^2\sin^2\theta\sin\phi$$

$$c_2 = c_1$$

$$a_3 = r_\theta^2\sin^2\theta + rr_{\theta\theta}\sin^2\theta + 2rr_\theta\sin\theta\cos\theta + 2rr_\theta\sin\theta\cos\theta$$
$$+ r^2\cos^2\theta - r^2\sin^2\theta$$

$$b_3 = rr_\theta\sin^2\theta + r^2\sin\theta\cos\theta$$

$$c_3 = c_1. \tag{39}$$

B.3. Moment of inertia tensor

After completing the r integral in Eq. (26), the components of the moment of inertia tensor, for a uniform density particle, in terms of the spherical harmonic expansion, are:

$$I_{11} = \frac{M}{5V}\int_0^{2\pi}\int_0^\pi r^5(\theta,\phi)\sin(\theta)[1 - \sin^2(\theta)\cos^2(\phi)]d\theta d\phi$$

$$I_{22} = \frac{M}{5V}\int_0^{2\pi}\int_0^\pi r^5(\theta,\phi)\sin(\theta)[1 - \sin^2(\theta)\sin^2(\phi)]d\phi d\theta$$

$$I_{33} = \frac{M}{5V}\int_0^{2\pi}\int_0^\pi r^5(\theta,\phi)\sin^3(\theta)d\theta d\phi$$

$$I_{12} = \frac{-M}{5V}\int_0^{2\pi}\int_0^\pi r^5(\theta,\phi)\sin^3(\theta)\cos(\phi)\sin(\phi)d\theta d\phi$$

$$I_{13} = \frac{-M}{5V}\int_0^{2\pi}\int_0^\pi r^5(\theta,\phi)\cos(\theta)\sin^2(\theta)\cos(\phi)d\phi$$

$$I_{23} = \frac{-M}{5V}\int_0^{2\pi}\int_0^\pi r^5(\theta,\phi)\cos(\theta)\sin^2(\theta)\sin(\phi)d\phi. \tag{40}$$

Appendix C. Exact equations for ellipsoids of revolution

This appendix gives the exact analytical formulae for ellipsoids of revolution for volume, surface area, moment of inertia, and integrated mean curvature [38].

For any ellipsoid with semiaxes a, b, and c, the volume is simply given by $V = (4/3)\pi abc$. In the case of ellipsoids of revolution, where $a = b$, this becomes $V = (4/3)\pi a^2 c$.

For the other three quantities, let $\eta = c/a$. For prolate ellipsoids, $\eta > 1$, while for oblate ellipsoids, $\eta < 1$. For prolate ellipsoids, the surface area is:

$$S_A = 2\pi a^2 \left[1 + \frac{\eta^2}{(\eta^2 - 1)^{-1/2}} \cos^{-1}(1/\eta) \right] \tag{41}$$

while for oblate ellipsoids:

$$S_A = 2\pi a^2 \left[1 + \frac{\eta^2}{(\eta^2 - 1)^{-1/2}} \cosh^{-1}(1/\eta) \right] \tag{42}$$

The integrated mean curvature for the prolate ellipsoid, without the surface area normalization, is:

$$hS_A = 2\pi a [\eta + (\eta^2 - 1)^{-1/2} \cosh^{-1}(\eta)] \tag{43}$$

while for the oblate ellipsoid, it is:

$$hS_A = 2\pi a [\eta + (1 - \eta^2)^{-1/2} \cos^{-1}(\eta)]. \tag{44}$$

The moment of inertia tensor, because of the symmetry of an ellipsoid of revolution with uniform density, has only three non-zero elements, $I_{11} = I_{22}$ and I_{33}. If semiaxis c is along the z direction, and semiaxes $a = b$ are along the x and y directions, then I_{11} corresponds to spinning about the x- or y-axis, and I_{33} corresponds to spinning about the z-axis. Spinning around the z-axis is the easiest way to spin for the prolate ellipsoid, and the hardest way to spin for the oblate ellipsoid. The diagonal elements of the moment of inertia tensor are given in terms of the semiaxes. For both kinds of ellipsoids,

$$I_{11} = I_{22} = \frac{M}{5}(a^2 + c^2), I_{33} = \frac{2M}{5}(a^2). \tag{45}$$

References

[1] J. Beddow (Ed.), Particle Characterization in Technology, CRC Press, Boca Raton, FL, 1984.

[2] B. Mather, Shape, surface texture, and coatings, Significance of Tests and Properties of Concrete and Concrete Aggregates, ASTM STP 169, American Society of Testing Materials, Philadelphia, 1955, pp. 284–296;
ASTM STP 169A, American Society of Testing Materials, Philadelphia, 1966, pp. 415–431.

[3] J.C. Russ, The Image Analysis Handbook, third ed., CRC Press, Boca Raton, FL, 1998.

[4] J. Serra, Image Analysis and Mathematical Morphology, Academic Press, New York, 1982.

[5] M.A. Taylor, Quantitative measures for shape and size of particles, 2001, preprint.

[6] A. Gray, Modern Differential Geometry of Curves and Surfaces, CRC Press, Boca Raton, FL, 1993.

[7] H. Goldstein, Classical Mechanics, Addison-Wesley, Reading, MA, 1950.

[8] J.F. Douglas, E.J. Garboczi, Intrinsic viscosity and polarizability of particles having a wide range of shapes, Adv. Chem. Phys. 91 (1995) 85–153.

[9] E.J. Garboczi, J.F. Douglas, Intrinsic conductivity of objects having arbitrary shape and conductivity, Phys. Rev. E 53 (1996) 6169–6180.

[10] J.F. Douglas, H.-X. Zhou, J.B. Hubbard, Hydrodynamic friction and the capacitance of arbitrarily shaped objects, Phys. Rev. E 49 (1994) 5319–5331.

[11] J.F. Douglas, A. Friedman, Coping with complex boundaries, in: A. Friedman (Ed.), Mathematics of Industrial Problems vol. 7, Springer-Verlag, New York, 1994, pp. 166–170.

[12] E.J. Garboczi, K.A. Snyder, J.F. Douglas, M.F. Thorpe, Geometrical percolation threshold of overlapping ellipsoids, Phys. Rev. E 52 (1995) 819–828.

[13] P. Meakin, A historical introduction to computer models for fractal aggregates, J. Sol–Gel Sci. Technol. 15 (1999) 97–117.

[14] D.P. Bentz, Three-dimensional computer simulation of Portland cement hydration and microstructure development, J. Am. Ceram. Soc. 80 (1997) 3–21 (See also http://vcctl.cbt.nist.gov).

[15] D.P. Bentz, E.J. Garboczi, K.A. Snyder, A hard-core soft-shell microstructural model for studying percolation and transport in three-dimensional composite media, NIST Internal Report 6265, December, 1999. Also found at http://ciks.cbt.nist.gov/monograph, Part I, Chapter 6, Section 8.

[16] J. Vieillard-Baron, Phase transitions of the classical hard-ellipse system, J. Chem. Phys. 56 (1972) 4729–4744.

[17] J.W. Perram, M.S. Wertheim, Statistical mechanics of hard ellipsoids: I. Overlap algorithm and the contact function, J. Comp. Phys. 58 (1985) 409–416.

[18] D.P. Bentz, J.T.G. Hwang, C. Hagwood, E.J. Garboczi, K.A. Snyder, N. Buenfeld, K.L. Scrivener, Interfacial zone percolation in concrete: Effects of interfacial zone thickness and aggregate shape, S. Diamond, S. Mindess, F.P. Glasser, L.W. Roberts (Eds.), Microstructure of Cement-Based Systems/Bonding and Interfaces in Cementitious Materials, vol. 370. Materials Research Society, Pittsburgh, 1995, pp. 437–442.

[19] N.L. Max, E.D. Getzoff, Spherical harmonic molecular surfaces, IEEE Comp. Graph. Appl. 8 (1988) 42–50.

[20] D.W. Ritchie, G.J.L. Kemp, Fast computation, rotation, and comparison of low resolution spherical harmonic molecular surfaces, J. Comp. Chem. 20 (1999) 383–395.

[21] B.S. Duncan, A.J. Olson, Approximation and characterization of molecular surfaces, Biopolymers 33 (1993) 219–229.

[22] M.T. Zuber, D.E. Smith, A.F. Cheng, J.B. Garvin, O. Aharonson, T.D. Cole, P.J. Dunn, Y. Guo, F.G. Lemoine, G.A. Neumann, D.D. Rowlands, M.H. Torrence, The shape of 433 Eros from the NEAR-Shoemaker laser rangefinder, Science 289 (2000) 1788–1793 (For further details of the spherical harmonic analysis and some interesting visuals, see http://sebago.mit.edu/near/nlr.30day.html.).

[23] W. Kaula, Theory of Satellite Geodesy, Dover, New York, 1960; Geodesy for the Layman, Defense Mapping Agency Technical Report, 1983. Available at http://geodesy.eng.ohio-state.edu/course/refpapers/NIMA.pdf.

[24] L. Wang, PhD thesis, Georgia Institute of Technology, 1997.

[25] P.E. Roelfstra, H. Sadouki, F.H. Wittmann, Le beton numerique, Mater. Struct. 18 (1985) 327–335.

[26] F.H. Wittmann, P.E. Roelfstra, H. Sadouki, Simulation and analysis of composite structures, Mater. Sci. Eng. 68 (1984) 239–248.

[27] N. Kiryati, D. Maydan, Calculating geometric properties from Fourier representation, Pattern Recognit. 22 (1989) 469–475.

[28] J.B. Scarborough, Numerical Mathematical Analysis, Johns Hopkins Press, Baltimore, 1966.

[29] L. Leithold, The Calculus with Analytical Geometry, Harper and Row, New York, 1976.

[30] B.P. Flannery, H.W. Deckman, W.G. Roberge, K.L. D'Amico, Three-dimensional X-ray microtomography, Science 237 (1987) 1439–1443.

[31] E.J. Garboczi, N.S. Martys, R.A. Livingston, H.S. Saleh, Acquiring, analyzing, and using complete three-dimensional aggregate shape information, in Proceedings of the Ninth Annual Symposium of the International Center for Aggregate Research, Austin, TX, 2001 (on CD and at http://ciks.cbt.nist.gov/monograph, Part I, Chapter 10, Section 3).

[32] K.R. Castleman, Digital Image Processing, Prentice-Hall, Englewood Cliffs, NJ, 1979.

[33] E.J. Garboczi, M.F. Thorpe, M. DeVries, A.R. Day, Universal conductivity curve for a plane containing random holes, Phys. Rev. A 43 (1991) 6473–6482.

[34] G. Arfken, Mathematical Methods for Physicists, second ed., Academic Press, New York, 1970.

[35] L.I. Schiff, Quantum Mechanics, McGraw-Hill, New York, 1968 (See Section 14).

[36] E.W. Hobson, The Theory of Spherical and Ellipsoidal Harmonics, Cambridge Univ. Press, Cambridge, 1931.

[37] SLATEC Common Mathematical Library, version 4.1 (1993). SLATEC stands for Sandia-Los Alamos-Air Force Weapons Laboratory-Technical-Exchange-Committee, available at http://gams.nist.gov/HOTGAMS/.

[38] K.M. Jansons, C.G. Phillips, On the application of geometric probability theory to polymer networks and suspensions I, J. Colloid Interface Sci. 137 (1990) 75–93.

[39] J.M. Rallison, S.E. Harding, Excluded volume for pairs of triaxial ellipsoids at dominant Brownian motion, J. Colloid Interface Sci. 103 (1985) 284–291.

[40] A. Isihara, Determination of molecular shape by osmotic measurement, J. Chem. Phys. 18 (1950) 1446–1449.

[41] http://vcctl.cbt.nist.gov, see Cement Image Database.

[42] http://vcctl.cbt.nist.gov.

[43] E.J. Garboczi, D.P. Bentz, N.S. Martys, Digital images and computer modeling, in: P. Wong (Ed.), Experimental Methods for Porous Media, Academic Press, New York, 1999, pp. 1–41.

[44] E.J. Garboczi, J.E. Taylor, A.P. Roberts, Analytical and computational aspects of surface energy-induced strain in models of porous materials, Proc. R. Soc. London, 2002 (submitted).